

Systematic Study of Monolayer to Trilayer CrI₃: Stacking Sequence Dependence of Electronic Structure and Magnetism

Published as part of The Journal of Physical Chemistry virtual special issue "D. D. Sarma Festschrift".

Duo Wang and Biplab Sanyal*

Cite This: *J. Phys. Chem. C* 2021, 125, 18467–18473

Read Online

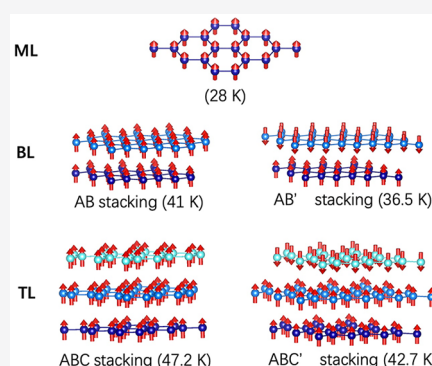
ACCESS |

Metrics & More

Article Recommendations

Supporting Information

ABSTRACT: In recent years, two-dimensional magnetic materials have attracted a lot of attention due to their unique magnetic properties, which can be manipulated by various degrees of freedom in a van der Waals stacked heterostructure, where different interlayer stackings affect the properties in different ways by exploiting weak interlayer interactions. An interesting example is CrI₃, where the interlayer magnetic coupling can be determined by the stacking sequence. Here we present a systematic study of the magnetic properties of monolayer, bilayer, and trilayer CrI₃ by using density functional theory and Monte Carlo simulations. The effects of different stacking sequences and the number of layers on the magnetic interaction in multilayer CrI₃ have been critically analyzed. We have found that the antiferromagnetic interlayer coupling occurs with specific interlayer shifting, while intralayer exchange interactions increase with the number of layers. It is noteworthy that interlayer interactions are independent of the number of layers, whereas the magnetic ordering temperature rises with the increasing number of layers. Moreover, we present the Curie temperatures obtained from Monte Carlo simulations and adiabatic magnon spectra for all the stacking sequences considered here.



INTRODUCTION

Theoretically, two-dimensional (2D) magnetic materials should not exist at a finite temperature due to the celebrated Mermin-Wagner theorem,¹ which tells us that the long-range magnetic order at any finite temperature will be completely destroyed by thermal spin fluctuations. However, this theoretical prediction is based on a 2D isotropic Heisenberg model, and when there is magnetic anisotropy, the restriction is removed, so there could be 2D Ising ferromagnetism. The family of layered metal halides² has varied magnetic states, including spin liquids,³ ultrathin insulating multiferroics,⁴ and ferromagnets and offer an enormous possibility to explore two-dimensional magnetism from the extraction of one or few monolayers. CrI₃ is a good example of such a material. In this regard, data driven materials discovery has played a very important role in predicting new 2D magnetic materials utilizing density functional theory and machine learning approaches.⁵

The bulk phase of CrI₃⁶ is a ferromagnet with out-of-plane spin orientation and a Curie temperature of 61 K. In 2017, a single atomic layer of CrI₃ was exfoliated from bulk crystal⁷ and it was found to have a Curie temperature of 45 K as well as out-of-plane easy axis of magnetization. Theoretical analysis has been carried out on the ferromagnetic ground state of monolayer CrI₃, for example, Kashin et al.⁸ found that the nearest-neighbor and next-nearest-neighbor exchange parameters play a dominant role, and there is a competition between

exchange parameters from different orbitals, which is mainly dependent on the orbital occupation. Very recently, Kvashnin et al.⁹ have shown the importance of relativistic exchange interactions in bulk and monolayer Cr-halides. Regarding multilayered CrI₃, both experiments and theories have revealed that the interlayer ground state magnetic configuration of multilayer CrI₃ is dependent on the external environment, such as magnetic field¹⁰ and external pressure.¹¹ Further studies have shown that different stacking sequences determine the magnetic ground state,^{12–16} which indicates that it is possible to tune the ferromagnetic and antiferromagnetic states of bilayer CrI₃ by changing the stacking sequence. Until now, few studies have investigated inter- and intralayer magnetic interactions by analyzing orbitally decomposed exchange parameters for a different number of layers and different stacking sequences.

In this paper, we systematically analyzed the interlayer magnetic interactions of bilayer and trilayer structures and obtained the dependence of the lateral shift of neighboring

Received: May 18, 2021

Revised: June 29, 2021

Published: August 13, 2021



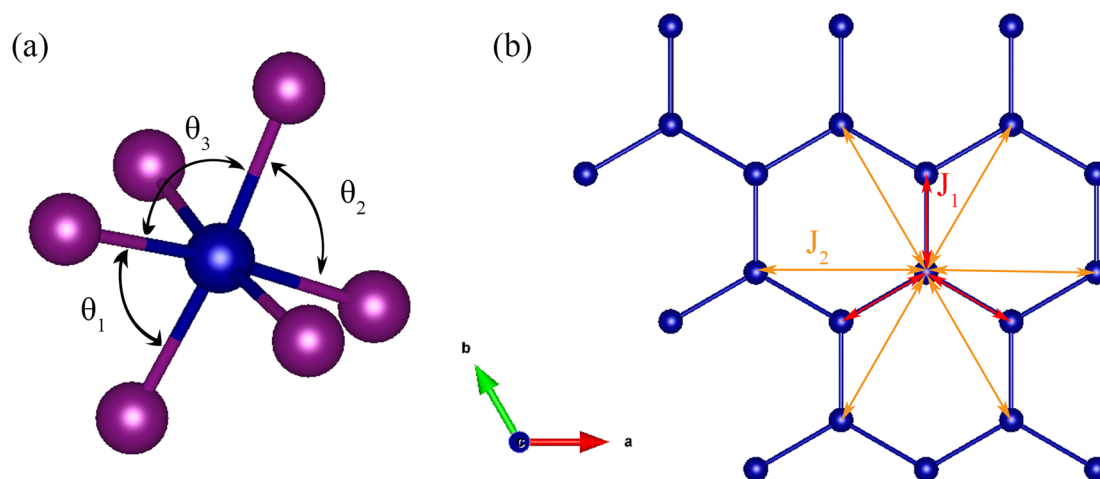


Figure 1. (a) CrI_6 octahedron and (b) schematic view of intralayer exchange parameters in monolayer CrI_3 .

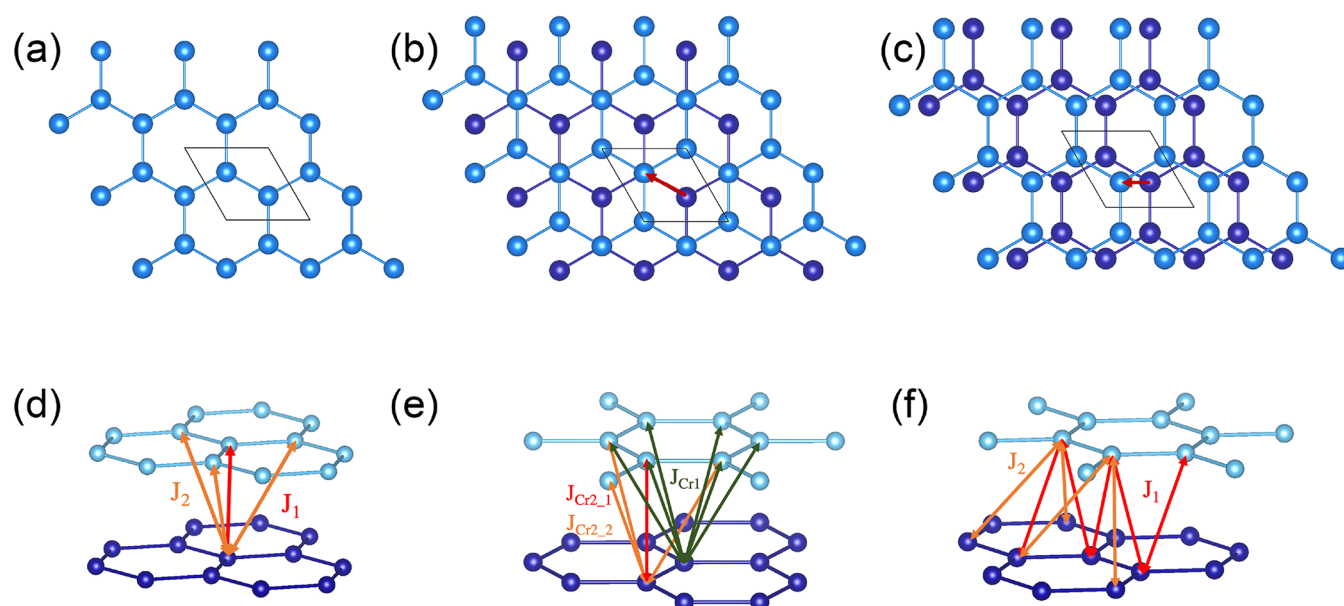


Figure 2. Cr lattice of bilayer CrI_3 . (a, d) AA; (b, e) AB; (c, f) AB'. Blue and cyan balls represent Cr atoms in the bottom and top layer. Red arrows in (b) and (c) indicate the direction of lateral shift. Arrows in (d), (e), and (f) represent examples of the first and second nearest Cr–Cr pairs.

layers on the magnetic interlayer interactions. Moreover, we observed the pattern of magnetic exchange parameters as a function of number of layers: first, the intralayer exchange parameters increase with the number of layers changing from a single layer to a trilayer; second, the interlayer exchange parameters have different values depending on the way of interlayer shifting, and they are relatively independent with respect to the number of layers. In addition, we used the calculated magnetic exchange parameters to further calculate the variation of Curie temperature with an increasing number of CrI_3 layers. A trend consistent with the experiments has been obtained.

COMPUTATIONAL DETAILS

Our computational approach is based on first-principles electronic structure calculations within density functional theory (DFT).¹⁷ We first performed a full structural relaxation through the projector augmented wave (PAW) method,^{18,19} as implemented in the VASP code.²⁰ The plane-wave energy cutoff was set to 450 eV, and the forces on the atoms were

minimized to 0.001 eV/Å. The k-integration in the Brillouin zone was performed using $8 \times 8 \times 1$ points for geometry optimization and $12 \times 12 \times 1$ points for self-consistent calculations. The TS-correction on PBE (DFT-TS) for van der Waals interaction was used in our geometry optimization as suggested in ref 16. The optimized structure was used as an input for the calculations of interatomic exchange parameters J_{ij} s by means of the magnetic force theorem (MFT)²¹ using full-potential linear muffin-tin orbital (FP-LMTO) code RSPt.²² To describe the exchange-correlation effects, we use the generalized gradient approximation (GGA)²³ augmented by the Hubbard-U corrections (GGA+U)^{24,25} with a U_{eff} value of 3 eV for the Cr-d electrons. Finally, we used the extracted J_{ij} s to calculate the magnetic ordering temperatures by classical Monte Carlo (MC) simulations with a Heisenberg Hamiltonian as implemented in the UppASD code.²⁶ In our simulation, the system size ranged from $10 \times 10 \times 1$ to $20 \times 20 \times 1$ with periodic boundary conditions, and five ensembles were used to properly average the properties.

RESULTS AND DISCUSSION

Structural Properties and Electronic Structure. In monolayer CrI_3 , the magnetic Cr ions form a honeycomb lattice, with each Cr atom coordinated by six I atoms that form a distorted edge-sharing octahedron. The point group of the monolayer CrI_3 is D_{3d} . The distorted octahedron and the Cr honeycomb lattices are shown in Figure 1.

Bulk CrI_3 forms a layered structure with monolayers separated by the vdW gap. Bulk CrI_3 has a low-temperature (below 210 K) phase with space group $R\bar{3}$ and a room-temperature phase with space group $C2/m$. The low-temperature phase has an ABC stacking with each layer laterally shifted by $[-1/3, 1/3]$ in fractional coordinates with respect to the lower neighboring layer. The high-temperature phase is associated with a relative shift of $[1/3, 0]$. Thus, both $R\bar{3}$ and $C2/m$ phases have an ABC stacking sequence. To distinguish the two cases, we refer to the $R\bar{3}$ phase as the ABC-stacking sequence and the $C2/m$ phase as the AB'C'-stacking sequence. For structural models of bilayer CrI_3 , we built structures with AB and AB' stacking sequences according to the lateral shift mentioned above. For comparison, we also built an AA stacked structure by putting a single layer CrI_3 on top of lower neighboring layer. The Cr lattices for these three structures are shown in Figure 2. For structural models of trilayer CrI_3 , we built nine different structures based on three basic combinations that come from our structural models for bilayer CrI_3 . The Cr lattices are shown in Figure S1 in the Supporting Information.

First, we performed geometry optimization for all of these structures, and for multilayer models, we did simulations with different interlayer magnetic orders. The calculated relative energies are shown in Tables 1 and 2. For monolayer CrI_3 , as

Table 1. Energies Relative to the Ground State (Shown in Bold) for the Bilayer CrI_3 , meV per Unit Cell^a

	AA	AB	AB'
$\uparrow\downarrow$	49.6	8.9	5.4
$\uparrow\uparrow$	47.7	0.0	5.5

^aThe closely lying energies are also indicated in bold.

shown in Figure 1a, there are three different I–Cr–I bond angles due to the distorted octahedron. Detailed structural data are provided in Table S1 in the Supporting Information.

For the bilayer CrI_3 , we note that while AB-stacking is at the global minimum, the energy of AB'-stacking is comparable to that of the AB-stacking. Hence, it is conceivable that the bilayer exfoliated at room-temperature may become kinetically trapped in AB'-stacking. It should be noted that the AB-stacking strongly prefers a FM coupling across the layers, while AB'-stacking is at the phase boundary between FM and AFM, but still in the domain of interlayer AFM coupling. Therefore, the dependence on the stacking order becomes obvious. For each trilayer CrI_3 structure, there are four different possible

interlayer magnetic orderings. The relative energies are shown in Table 2. The global minimum occurs for the ABC stacking with FM interlayer magnetic ordering, which is consistent with the experimental observation at a low temperature. The second lowest energy state belongs to the ABC' stacking with up–up–down spin configuration. The third lowest energy state occurs for the AB'C' stacking with up–down–up magnetic ordering, which is the high-temperature phase in experiment. These results are expected according to the results from bilayer CrI_3 : whenever there is a $[1/3, 0]$ lateral shift between neighboring layers, the AFM ordering is preferred.

Electronic Structure. Cr^{3+} ion has an electronic configuration of $3d^3$. In the octahedral environment, Cr d orbitals split into a set of three low energy t_{2g} orbitals, and two higher energy e_g orbitals. Therefore, according to Hund's rule, the three electrons occupying the t_{2g} triplet will have $S = 3/2$, which gives an atomic magnetic moment of $3 \mu_B$. This picture is consistent with the observed saturation magnetization of bulk CrI_3 . The calculated Cr spin magnetic moment in all the CrI_3 structures is $\sim 3.3 \mu_B$, being in good agreement with the experimental value.⁶ Interestingly, there is also a small induced magnetic moment ($0.14 \mu_B$) on the I atom, which is antiparallel to that of the Cr magnetic moment. All these results in a total magnetic moment of $3.00 \mu_B/\text{f.u.}$ for all the structures. As shown in the data of orbital occupation (Table 3), three t_{2g} orbitals of the spin-up channel are almost fully

Table 3. Calculated Orbital-Resolved Electron Occupations and Magnetic Moments for CrI_3 Monolayer^a

orbital	N_\uparrow	N_\downarrow	M
t_{2g}	2.79	0.06	2.73
e_g	0.86	0.28	0.58
d	3.65	0.34	3.31

^a \uparrow and \downarrow denote the up and down spins, respectively. The e_g and t_{2g} states are defined in each atomic local axis, unit in eV.

occupied (2.79), and because of the strong hybridization between Cr d orbital and I p orbital, there is 0.86 electron at the e_g orbitals.

In Figure 3, we show the spin-resolved band structures with relative contribution of I $2p$ shell and Cr $3d$ shell, indicated by the size of the circles. For both spin channels, the energy regions around the valence band maximum are dominated by I p orbitals, whereas the conduction band minimum is dominated by less dispersive Cr d orbitals. Also, it is seen that the energy gap in the spin down channel is bigger than the spin-up channel in this direct band gap semiconductor. The orbitally resolved band structures for other cases are shown in the Supporting Information. All the multilayered structures are observed to be direct band gap semiconductors.

As mentioned earlier, one of the important characteristic features of 2D magnets is the magnetic anisotropy. From the calculations of Magnetocrystalline Anisotropy Energy (MAE)

Table 2. Energies Relative to the Ground State (Shown in Bold) for the Trilayer CrI_3 , meV per Unit Cell

	AAA	AAB	AAB'	ABB	ABC	ABC'	AB'B'	AB'C	AB'C'
$\uparrow\uparrow\uparrow$	96.6	47.8	53.5	47.6	0.0	5.1	53.4	5.0	10.8
$\uparrow\uparrow\downarrow$	98.7	49.8	55.5	56.8	8.9	14.2	53.2	4.9	10.5
$\uparrow\downarrow\uparrow$	100.7	58.8	55.2	58.8	17.9	14.0	55.2	13.9	10.4
$\uparrow\downarrow\downarrow$	98.7	56.9	53.3	49.7	8.8	4.9	55.4	14.0	10.6

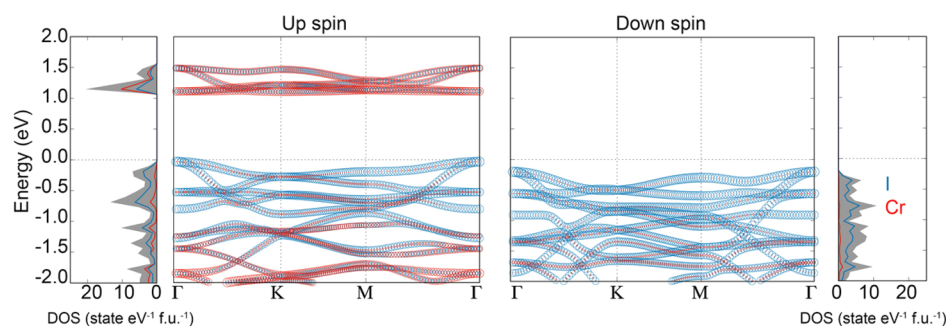


Figure 3. Spin and orbital resolved band structure and density of states of CrI₃ monolayer. The size of circles in the band structure is proportional to the weight of the respective orbital. In each panel, the dashed line at zero energy indicates the Fermi level.

taking into account spin–orbit coupling, we observe that the easy magnetization direction is always along the *z* axis in agreement with experimental observations. Our calculated orbital moments are 0.07 and 0.06 μ_B for in-plane and out-of-plane magnetization directions, respectively. Figure 4 shows

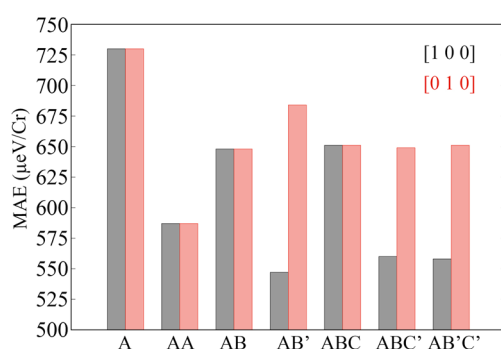


Figure 4. Calculated MAEs obtained from the total energy differences for different stacking sequences.

that the MAEs are large, and do not vary much with film thickness. Besides that, as we can see from the MAE results of AB', ABC', and AB'C' structures, whenever a $[1/3, 0]$ lateral shift occurs, the magnetic anisotropy energies along $[100]$ and $[010]$ direction are no longer equivalent due to further symmetry breaking.

Interatomic Exchange Parameters. The calculated interatomic exchange interactions in CrI₃ monolayer, including total and orbital decomposed, are presented in Figure 5a. The first two nearest Cr–Cr pairs significantly contribute to the FM state, the values being 1.020 and 0.544 meV, respectively. In

contrast, the longer-ranged interactions ($R_{ij}/a > 3$) are negligibly small due to the presence of a semiconducting gap in both spin channels. The dominant contribution comes from FM e_g – t_{2g} channels. The e_g – e_g and t_{2g} – t_{2g} orbital interactions are AFM, but the difference is that these two interactions decrease drastically so that the second nearest-neighbor couplings contributed by these two channels are almost zero.

As Cr is trivalent and in an octahedral environment and the Cr–I–Cr angle is close to 90°, hopping of the form t_{2g} – t_{2g} is prohibited for FM alignment, whereas this is allowed for AFM alignment; therefore, the t_{2g} – t_{2g} hybridization leads to an AFM configuration. On the other hand, hopping of the form t_{2g} – e_g leads to an exchange coupling that is FM because of the local Hund's coupling. This intralayer FM coupling is through a FM Cr–I–Cr superexchange, in which the Cr–I–Cr bond angle (93°) approaches 90°. It is remarkable that e_g orbitals play an important role, which should be magnetically inactive in the pure ionic picture of Cr³⁺. This is also understandable as shown in Table 3, the e_g states carry sizable moments due to the hybridization with I *p* orbitals. This detailed microscopic information provides unique insights into the understanding the magnetism of this material.

Compared to the data of J_{ij} for each Cr–Cr pair, a more intuitive approach would be to plot a figure by summing all the J_{ij} pairs reflecting the corresponding coordination number. For a Cr atom in monolayer CrI₃, there are three first-neighbor and six second-neighbor couplings for which the summed up J_{ij} s are shown in Figure 5b. It is observed that the FM contribution of the second nearest neighbor is even larger than that of the first nearest neighbor ($J_1 = 3.075$ meV and $J_2 = 3.293$ meV, respectively).

It is worth noting that, for the multilayer stacked CrI₃, the stacking affects the intralayer J_{ij} . The results for the bilayer

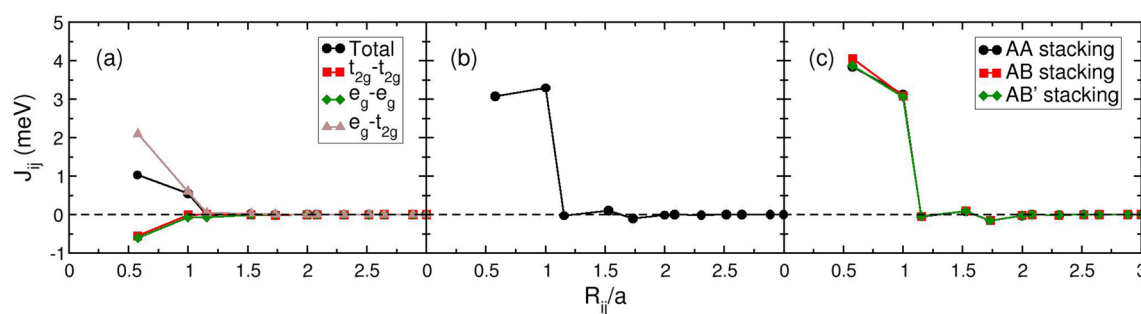


Figure 5. Intralayer exchange parameters (a) (total and orbitally resolved) of monolayer CrI₃ for each pair, (b) summed over all neighboring pairs of monolayer CrI₃ and (c) summed over all neighboring pairs for bilayer structures with different stackings. Positive number indicates FM contribution, and negative means AFM.

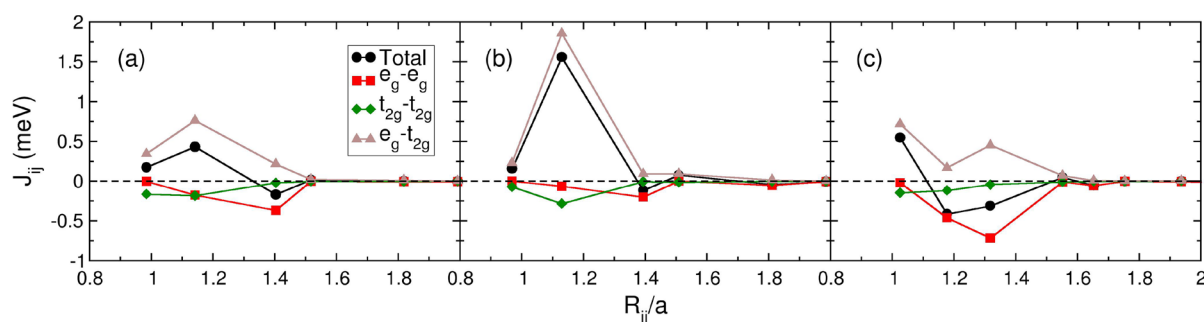


Figure 6. Interlayer exchange parameters (summed over neighbors) of bilayer CrI_3 with different stacking sequences: AA (a), AB (b), and AB' (c).

structures are shown in Figure 5c for different stacking sequences. The summed first nearest exchange parameter (J_1) has increased from 3.075 to 3.837, 4.055, and 3.878 meV for AA, AB', and AB stacking, respectively. The summed second nearest neighbor coupling has decreased from 3.293 to 2.993 meV.

Now we discuss the interlayer exchange couplings for different stacking sequences in bilayer structures. Due to the change of hopping routes as well as the different numbers of neighboring sites, the orbital interaction profile is notably different in three structures. For the ground state bilayer CrI_3 (AB stacking with FM interlayer magnetic ordering), the calculated interlayer coupling is FM; there is one nearest, nine next-nearest, and 12 third-nearest couplings. These results are shown in Figure 6b. The nearest neighbor J_1 and the second neighbor J_2 are both FM, whereas the long-range interactions ($J_n > 3$) are negligibly small. The dominant contribution comes from FM e_g-t_{2g} channels. The e_g-e_g and $t_{2g}-t_{2g}$ orbital interactions are AFM but significantly weaker. For the second-lowest energy state (AB' stacking), the calculated interlayer coupling is AFM. There are four nearest, four next-nearest, and eight third-nearest neighbor couplings. The nearest neighbor J_1 is FM, but interestingly, the second and the third nearest neighbor interactions are AFM. We investigated the orbitally decomposed exchange parameters, although the e_g-t_{2g} interactions of J_2 are still FM, but significantly weaker. As a result, J_2 becomes AFM in the AB' stacked structure. It is also noted that coupling for the third-nearest neighbors (J_3) is sizable when we compare it to the J_2 , this bigger magnitude is largely due to the enhanced AFM coupling of the e_g-e_g channel.

For the sake of comparison, we also looked at the AA stacked bilayer CrI_3 . The calculated interlayer coupling is FM. There are two nearest, six next-nearest, and 12 third-nearest neighbor couplings for each Cr atom. The changing trend of J_{total} and also three orbitally resolved channels is the same as the trend in AB-stacked CrI_3 . The difference is that there the values are smaller in the e_g-t_{2g} channel due to different hopping routes. Microscopically, the magnetic interaction and the ground-state spin order of bilayer CrI_3 can be understood from the competition and the cooperation of FM $J_{e_g-t_{2g}}$, AFM $J_{e_g-e_g}$, and AFM $J_{t_{2g}-t_{2g}}$ couplings. A lateral shift of one monolayer with respect to the other breaks the interlayer hybridization between I p states and generates new ones.

It is interesting when we investigate results from the trilayer CrI_3 . These are presented in the Supporting Information. As shown in Figure S4, the first nearest-neighbor intralayer exchange coupling has increased for three trilayer structures, but there are two things that are different from the changes

that happened in bilayer CrI_3 . First, the two Cr atoms, which are in the same layer, are not equivalent anymore, as shown in the values of exchange parameters. Second, the exchange parameters of the layer in the middle have increased more than other layers. J_1 has increased to 4.708, 4.544, and 4.368 meV for ABC, ABC', and AB'C', respectively (compared to 3.075 meV for the CrI_3 monolayer). Interlayer exchange parameters of trilayer CrI_3 are shown in Figure S5 of the Supporting Information for ABC stacking. It can be seen that the values of the interlayer exchange parameters are the same for all AB-like stacking structures and do not change with increasing numbers of layers. For the AB'-type stacking structure, there is only a subtle change in the values. Compared to the intralayer exchange parameters, the interlayer exchange coupling is rather weak. That is because two successive hoppings (Cr–I–I–Cr) are required for the magnetic interaction of this 2D vdW material. It suggests that a much weaker interlayer coupling allows the magnetism to be more feasibly tuned.

Calculated magnetic ordering temperatures from Monte Carlo simulations are shown in Figure 7. As the number of

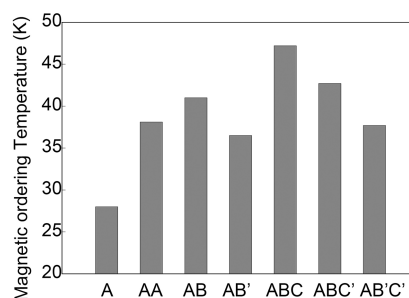


Figure 7. Magnetic ordering temperatures of monolayer (A), bilayer (AA, AB, AB'), and trilayer (ABC, ABC', AB'C') CrI_3 .

layers increases, the magnetic ordering temperature increases. This trend is obvious for the three ground-state structures. For the monolayer structure, the bilayer structure with AB stacking, and the trilayer structure with ABC stacking, the calculated Curie temperatures are 28.0, 41.0, and 47.2 K, respectively. This is consistent with the experimentally observed Curie temperatures of monolayer and bulk CrI_3 as 45 and 61 K, respectively. In addition, there is an effect of different stacking order on the magnetic ordering temperature. The structures with purely AB-like stacking (AB and ABC in Figure 7) have the highest Curie temperature, while the presence of AB'-like stacking (AB', ABC', and AB'C' in Figure 7) results in a slight decrease in the ordering temperature. This can be explained by the stronger second-nearest neighbor FM coupling in AB-like stacked structures.

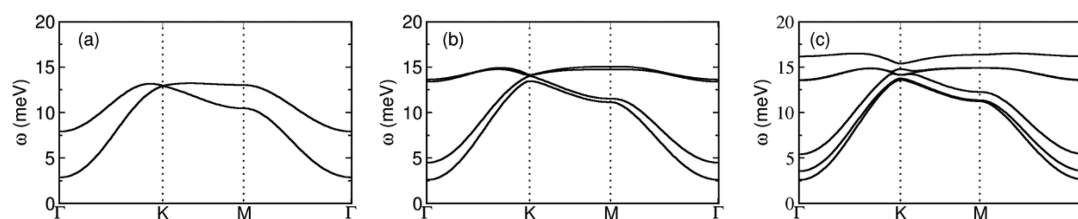


Figure 8. Adiabatic magnon spectra of CrI_3 (a) monolayer, (b) bilayer, and (c) trilayer. For bilayer and trilayer, the most stable structures have been considered.

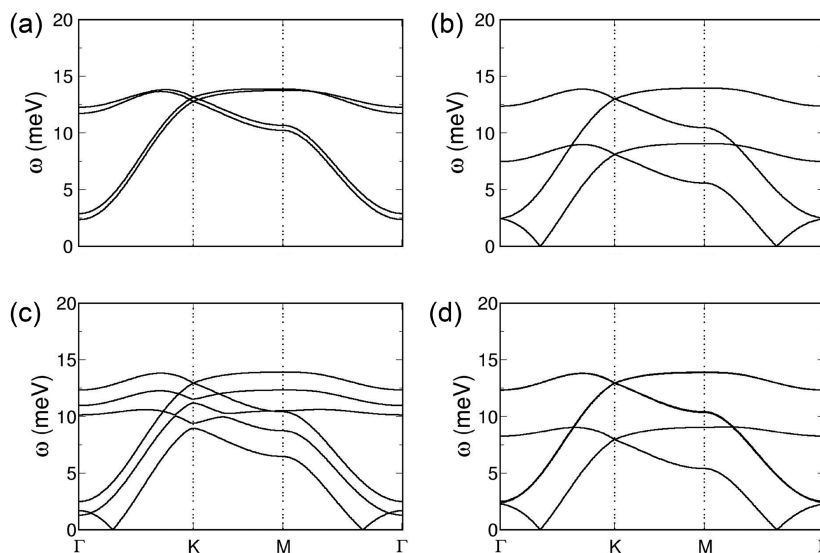


Figure 9. Adiabatic magnon spectra of bilayer and trilayer CrI_3 (a) with different stacking sequences: AA (a), AB' (b), ABC' (c), $\text{AB}'\text{C}'$ (d).

We have also calculated the adiabatic magnon dispersion for monolayer, bilayer, and trilayer. They are shown in Figure 8 for the ground state ferromagnetic structures. Some general features can be observed. First, in all the cases there is a finite gap in the acoustic magnon mode at the Γ point. The values of the energy gaps are between 2.61 and 2.88 meV, which are directly related to the values of MAE. It also implies that the acoustic magnon properties are determined by out-of-plane magnetic anisotropy, which is consistent with the experimental result.²⁷ Second the quadratic dependence of magnon dispersion indicates a ferromagnetic ordering. For the monolayer case, the two branches become degenerate at the K point. This is also observed in the bilayer case. The number of branches is dictated by the number of Cr atoms in the unit cell. Therefore, the monolayer, bilayer and trilayer have 2, 4, and 6 branches of which some of them are degenerate. Furthermore, in the bilayer and trilayer structures, there are optical magnon modes at around 15 meV, which is also consistent with the observation in experiment.²⁷ It is also seen that the high frequency branches are less dispersive than the low frequency ones. The results for the metastable structures are shown in Figure 9. Interestingly, for structures which have lateral shift equals to $[-1/3, 0]$, such as AB' , ABC' , and $\text{AB}'\text{C}'$ stacking in Figure 9b–d, there is softening of one magnon branch around the Γ point, which might indicate magnetic instability in these structures.

CONCLUSION

To summarize, we systematically investigated the magnetic interactions in monolayer, bilayer, and trilayer CrI_3 . For each

stacking order, the ground state magnetic structure is determined by the competition between different orbital-dependent AFM and FM exchange interactions. We found that with two different lateral shifts, two magnetic interactions occur. These findings are consistent with the experimental results. The thickness of CrI_3 multilayer affects intralayer exchange interaction, while the intralayer exchange is more or less independent of it. Due to stronger e_g-t_{2g} interaction channels, the intralayer nearest neighbor exchange interactions (which is FM) increase with the increase in the number of stacked layers. Furthermore, as the result of these increased intralayer exchange couplings and extra interlayer interactions, the Curie temperature of the material increases as the number of layers increases. This result is consistent with the experimental results.

ASSOCIATED CONTENT

Supporting Information

The Supporting Information is available free of charge at <https://pubs.acs.org/doi/10.1021/acs.jpcc.1c04311>.

Structural information for different magnetic structures, band structures for different stackings, and intralayer and interlayer exchange parameters for various stackings (PDF)

AUTHOR INFORMATION

Corresponding Author

Biplab Sanyal – Department of Physics and Astronomy, Uppsala University, 75120 Uppsala, Sweden; orcid.org/

0000-0002-3687-4223; Email: biplab.sanyal@physics.uu.se

Author

Duo Wang — Department of Physics and Astronomy, Uppsala University, 75120 Uppsala, Sweden

Complete contact information is available at:
<https://pubs.acs.org/10.1021/acs.jpcc.1c04311>

Notes

The authors declare no competing financial interest.

ACKNOWLEDGMENTS

We thank Y. Kvashnin, A. Bergman, and M. Pereiro for useful discussions. D.W. acknowledges the China scholarship council for financial support (No. 201706210084). B.S. acknowledges the financial support from the project grant (2016-05366) and Swedish Research Links programme grant (2017-05447) from Swedish Research Council and Carl Tryggers Foundation. We also acknowledge SNIC-UPPMAX, SNIC-HPC2N, and SNIC-NSC centers under the Swedish National Infrastructure for Computing (SNIC) resources and PRACE DECI-15 Project DYNAMAT for the allocation of time in high-performance supercomputers.

REFERENCES

- (1) Mermin, N. D.; Wagner, H. Absence of Ferromagnetism or Antiferromagnetism in One- or Two-Dimensional Isotropic Heisenberg Models. *Phys. Rev. Lett.* **1966**, *17*, 1133–1136.
- (2) McGuire, M. A. Crystal and Magnetic Structures in Layered, Transition Metal Dihalides and Trihalides. *Crystals* **2017**, *7*, 121.
- (3) Banerjee, A.; Yan, J.; Knolle, J.; Bridges, C. A.; Stone, M. B.; Lumsden, M. D.; Mandrus, D. G.; Tennant, D. A.; Moessner, R.; Nagler, S. E. Neutron scattering in the proximate quantum spin liquid -RuCl_3 . *Science* **2017**, *356*, 1055–1059.
- (4) Kurumaji, T.; Seki, S.; Ishiwata, S.; Murakawa, H.; Tokunaga, Y.; Kaneko, Y.; Tokura, Y. Magnetic-Field Induced Competition of Two Multiferroic Orders in a Triangular-Lattice Helimagnet MnI_2 . *Phys. Rev. Lett.* **2011**, *106*, 167206.
- (5) Rhone, T. D.; Chen, W.; Desai, S.; Torrisi, S. B.; Larson, D. T.; Yacoby, A.; Kaxiras, E. Data-driven studies of magnetic two-dimensional materials. *Sci. Rep.* **2020**, *10*, 15795.
- (6) McGuire, M. A.; Dixit, H.; Cooper, V. R.; Sales, B. C. Coupling of Crystal Structure and Magnetism in the Layered, Ferromagnetic Insulator CrI_3 . *Chem. Mater.* **2015**, *27*, 612–620.
- (7) Huang, B.; Clark, G.; Navarro-Moratalla, E.; Klein, D. R.; Cheng, R.; Seyler, K. L.; Zhong, D.; Schmidgall, E.; McGuire, M. A.; Cobden, D. H.; et al. Layer-dependent ferromagnetism in a van der Waals crystal down to the monolayer limit. *Nature* **2017**, *546*, 270–273.
- (8) Kashin, I. V.; Mazurenko, V. V.; Katsnelson, M. I.; Rudenko, A. N. Orbital-resolved ferromagnetism of monolayer CrI_3 . *2D Mater.* **2020**, *7*, 025036.
- (9) Kvashnin, Y. O.; Bergman, A.; Lichtenstein, A. I.; Katsnelson, M. I. Relativistic exchange interactions in CrX_3 ($X = \text{Cl}, \text{Br}, \text{I}$) monolayers. *Phys. Rev. B: Condens. Matter Mater. Phys.* **2020**, *102*, 115162.
- (10) Xu, R.; Zou, X. Electric Field-Modulated Magnetic Phase Transition in van der Waals CrI_3 Bilayers. *J. Phys. Chem. Lett.* **2020**, *11*, 3152–3158.
- (11) Song, T.; Fei, Z.; Yankowitz, M.; Lin, Z.; Jiang, Q.; Hwangbo, K.; Zhang, Q.; Sun, B.; Taniguchi, T.; Watanabe, K.; et al. Switching 2D magnetic states via pressure tuning of layer stacking. *Nat. Mater.* **2019**, *18*, 1298–1302.
- (12) Li, T.; Jiang, S.; Sivadas, N.; Wang, Z.; Xu, Y.; Weber, D.; Goldberger, J. E.; Watanabe, K.; Taniguchi, T.; Fennie, C. J.; et al.

Pressure-controlled interlayer magnetism in atomically thin CrI_3 . *Nat. Mater.* **2019**, *18*, 1303–1308.

(13) Thiel, L.; Wang, Z.; Tschudin, M. A.; Rohner, D.; Gutiérrez-Lezama, I.; Ubrig, N.; Gibertini, M.; Giannini, E.; Morpurgo, A. F.; Maletinsky, P. Probing magnetism in 2D materials at the nanoscale with single spin microscopy. *Science* **2019**, *364*, 973–976.

(14) Sivadas, N.; Okamoto, S.; Xu, X.; Fennie, C. J.; Xiao, D. Stacking-Dependent Magnetism in Bilayer CrI_3 . *Nano Lett.* **2018**, *18*, 7658–7664.

(15) Jiang, P.; Wang, C.; Chen, D.; Zhong, Z.; Yuan, Z.; Lu, Z.-Y.; Ji, W. Stacking tunable interlayer magnetism in bilayer CrI_3 . *Phys. Rev. B: Condens. Matter Mater. Phys.* **2019**, *99*, 144401.

(16) Jang, S. W.; Jeong, M. Y.; Yoon, H.; Ryee, S.; Han, M. J. Microscopic understanding of magnetic interactions in bilayer CrI_3 . *Physical Review Materials* **2019**, *3*, 031001.

(17) Kohn, W.; Sham, L. J. Self-Consistent Equations Including Exchange and Correlation Effects. *Phys. Rev.* **1965**, *140*, A1133–A1138.

(18) Blöchl, P. E. Projector augmented-wave method. *Phys. Rev. B: Condens. Matter Mater. Phys.* **1994**, *50*, 17953–17979.

(19) Kresse, G.; Joubert, D. From ultrasoft pseudopotentials to the projector augmented-wave method. *Phys. Rev. B: Condens. Matter Mater. Phys.* **1999**, *59*, 1758–1775.

(20) Kresse, G.; Furthmüller, J. Efficiency of ab-initio total energy calculations for metals and semiconductors using a plane-wave basis set. *Comput. Mater. Sci.* **1996**, *6*, 15–50.

(21) Liechtenstein, A. I.; Katsnelson, M. I.; Antropov, V. P.; Gubanov, V. A. Local spin density functional approach to the theory of exchange interactions in ferromagnetic metals and alloys. *J. Magn. Magn. Mater.* **1987**, *67*, 65–74.

(22) Wills, J. M.; Alouani, M.; Andersson, P.; Delin, A.; Eriksson, O.; Grechnev, O. *Full-Potential Electronic Structure Method: Energy and Force Calculations with Density Functional and Dynamical Mean Field Theory*; Springer Science & Business Media, 2010; Vol. 167.

(23) Perdew, J. P.; Burke, K.; Ernzerhof, M. Generalized Gradient Approximation Made Simple. *Phys. Rev. Lett.* **1996**, *77*, 3865–3868.

(24) Anisimov, V. I.; Aryasetiawan, F.; Lichtenstein, A. I. First-principles calculations of the electronic structure and spectra of strongly correlated systems: the LDA + U method. *J. Phys.: Condens. Matter* **1997**, *9*, 767–808.

(25) Dudarev, S. L.; Botton, G. A.; Savrasov, S. Y.; Humphreys, C. J.; Sutton, A. P. Electron-energy-loss spectra and the structural stability of nickel oxide: An LSDA+U study. *Phys. Rev. B: Condens. Matter Mater. Phys.* **1998**, *57*, 1505–1509.

(26) Eriksson, O.; Bergman, A.; Bergqvist, L.; Hellsvik, J. *Atomistic Spin Dynamics: Foundations and Applications*; Oxford University Press, 2017.

(27) Cenker, J.; Huang, B.; Suri, N.; Thijssen, P.; Miller, A.; Song, T.; Taniguchi, T.; Watanabe, K.; McGuire, M. A.; Xiao, D.; Xu, X. Direct observation of two-dimensional magnons in atomically thin CrI_3 . *Nat. Phys.* **2021**, *17*, 20–25.